We are IntechOpen, the world's leading publisher of Open Access books Built by scientists, for scientists

4,800
Open access books available

122,000
International authors and editors

135M
Downloads

Our authors are among the

154
Countries delivered to

TOP 1%
most cited scientists

12.2%
Contributors from top 500 universities

WEB OF SCIENCE™

Selection of our books indexed in the Book Citation Index in Web of Science™ Core Collection (BKCI)

Interested in publishing with us?
Contact book.department@intechopen.com

Numbers displayed above are based on latest data collected.
For more information visit www.intechopen.com

7

Gas Trapping During Foamed Flow in Porous Media

Quoc P. Nguyen
The University of Texas at Austin
USA

1. Introduction

Two pore-scale constituents of foam mobility are effective yield stress and viscosity. These rheological quantities have been related directly to foam texture, flow rate, and morphology of the porous medium. It would be ideal to observe these relationships in natural rocks to capture more realistic foam behavior in the field. Since a technique for directly visualizing foam texture in natural porous media is not available, the interpretation of foam mobility on the basis of texture is impossible. Generally, all that is available is the measured pressure drop. Consider two typical foam processes commonly studied in the laboratory: liquid displacement by foam (LDF), and foam displacement by liquid (FDL). These processes represent many of the field applications of foam for gas/liquid mobility control.

Experimental study of local foam mobility does not seem to have been reported in literature. The few existing investigations on in-situ foam-induced fluid partitioning have provided only partial insight into the conditions for foam generation. Apaydin and Kovscek [2000] verified their "bubble population balance'' model by fitting the experimental one-dimensional pressure drop and fluid saturation profiles during the transient foam displacement in sandpacks. The local liquid saturation profiles were determined using an X-ray Computed Tomography (X-ray CT) technique. Wassmuth et al. [2001] conducted several foam-flood experiments, where distribution of local fluid saturations was visualized using a Magnetic Resonance Imaging (MRI) technique. The authors have not reported the corresponding pressure drop data, thus limiting the interpretation.

Although most of the reported experimental studies [Zerhboub et al., 1994; Parlar et al., 1995; Siddiqui et al., 1997; Behenna, 1995; Thompson and Gdanski, 1993] on the FDL process have been focused on the acid diversion process, their outcomes are expected be relevant for water shut-off by foam. The insight gained into the FDL process is mainly due to Rossen and co-workers [1994, 2001], who conducted systematic studies using two-stage experiments of foam placement followed by liquid injection. Rossen et al. [1994, 2001] found that the pressure gradient declines in two steps. The pressure gradient first falls rapidly, but levels off to a value that remains relatively high. This is followed by a rather gradual decrease that leads to a quasi-steady state of liquid flow in the presence of significant trapped foam. The authors explained their results using a picture of foam flow in porous media in which the foam is separated in two parts. A (small) fraction of the foam is mobile following a mechanism of lamellae displacement. The remaining part exists in the form of trapped bubbles. When liquid is injected into the porous medium containing foam, the

mobile bubbles are driven out which causes the pressure to drop steeply. The gas contained in the trapped bubbles then slowly expands and dissolves in the liquid and leads to the final gradual decline of the pressure gradient. The quasi-steady-state fraction of trapped gas was estimated using the pressure drop profile and the Darcy law for the liquid phase. The amount of stationary foam relates closely to the kinetics of foam generation by virtue of lamella mobilization and division. On the other hand, for foam displacement by liquid (FDL), the characteristic flow regime is liquid fingering, which reflects a wide spectrum of local foam mobility. This leads to a hypothesis that if the quasi-stationary foam domain observed during the FDL is approximately the same as that during the steady state foam flow, one can predict the structure of the liquid finger for known distribution of local foam mobility, and vice versa. However, the blocking/diverting capacity of foam depends on not only the trapped gas fraction, but also on the pattern of foam displacement by liquid. As we shall show later, these factors are not always correlated. The in-situ fluid partitioning profile is thus needed to strengthen the interpretation of the experiments. Note that most of the above studies on the LDF or FDL process used bead- and sandpacks, missing the important effect of natural rock layering.

This work is concerned with the macroscopic mechanisms of foam propagation, trapping and resistance to liquid flow, with a focus on the less-explored issues addressed above. For this purpose, a systematic investigation on both LDF and FDL processes was conducted through –CT-visualized, two-stage foam core-flood experiments: foam flood followed with liquid injection using the X-ray CT imaging technique and different types of sandstones. A new method for determining the distribution of local foam mobility during the macroscopically steady-state flow in sandstone cores was developed based on the X-Ray CT imaging technique and Xenon gas (Xe) as a visual tracer. Due to the enhanced X-ray absorption of the tracer, one can track the mobile foam and thus estimate the saturation of trapped foam. Beyond this, the results also provide insight into the convection-diffusion problems in porous media.

2. Experimental description

2.1 Principle and apparatus

a. Principle

A CT scan is a special type of X-ray that can reconstruct the cross-sectional internal structure of an object from multiple projections of the object. The latter represents the attenuation of X-rays through the object. Consider a parallel beam of X-ray photons with sufficiently small width propagating through a slab of a porous rock, which confines mobile and stationary nitrogen foams at the quasi-steady state. The slab is divided into regular voxels whose size is sufficiently small that they can represent the differential properties of the slab. The incident beam attenuates due to photons either being absorbed by the atoms of the materials (core-holder materials, rock, surfactant solution, and gas) or being scattered away from their original directions of travel. For a range of photon energies most commonly encountered in practice (from 20 to 150 keV), the mechanisms responsible for these two contributions to the attenuation are the photoelectric and the Compton effect. The former, (much more energy dependent than the latter), becomes dominant at energies below about 100 KeV. For convenience, these effects are customarily evaluated together through a single constant, $\hat{\mu}$, representing the attenuation coefficient of the material. Although it is customary to say that a CT scanner calculates the linear attenuation coefficient of the materials (at some effective

energy), the numbers actually put out by the computer attached to the scanner are integers, called the CT values. These values are measured in Hounsfield units, denoted by HU. The relationship between the linear attenuation coefficient and the corresponding Hounsfield unit HU is

$$HU_m(t,s,E_r) = \left(\frac{\hat{\mu}_m(t,s,E_r)}{\hat{\mu}_w(E_r)} - 1 \right) \times 1000 \tag{1}$$

where $\hat{\mu}_w(E_r)$ is the attenuation coefficient of water. The value HU_m = 0 corresponds to water; and the value HU_m = -1000 corresponds to $\hat{\mu}_m(t,s,E_r)$ = 0, which is assumed to be the attenuation coefficient of air ($\hat{\mu}_a$). Since the latter is difficult to obtain in practice, it is more convenient to use the following normalized form of HU_m (equivalent to liquid saturation S_w), assuming linearity between the measured HU_m and the actual value of the attenuation coefficient $\hat{\mu}_m$.

$$S_w = \frac{HU_m - HU_{mw}}{HU_{mw} - HU_{ma}} \times 1000 \tag{2}$$

where HU_{mw} and HU_{ma} are the measured Hounsfield units for water and air, respectively. Note that for those materials having atomic numbers higher than water, such as natural rocks, their CT values are far above zero. Assuming the linearity between HU and bulk density for this range of CT value, the contribution of rock to the total measured attenuation can be eliminated by the linear image subtraction algorithm [McCullough, 1975; Kak and Roberts, 1986]

b. X-ray CT scanner

The X-ray CT system used is of the fourth-generation SAMATOM AR produced by Siemens. For the whole object examinations, the X-ray source-detector system rotates continuously, utilizing the traversing slice method. The main technical data of this scanner is presented in Table 1.

Specification	Quantity
Max tube voltage	134 kV
Filtering	6.5 mm AL equivalent
Tube current range	50, 70, 100 mA
Projections per second	333
Number of channels	704, 1024
Scan time (seconds)	1.3, 1.9, 2, 3, 5 s
Scan field	28/45, 45
Table speed	0.5 - 100 mm/s ± 15%
Arbitrary tabletop movement	± 0.5 mm

Table 1. Main technical data of the X-ray CT system

The imaging system uses the Somaris software to reconstruct CT images from the measurement data received. However, we only use this system for monitoring real time propagation of the components during core floods and for obtaining online statistical data of the X-ray adsorption of the fluid system at steady states. A standalone image processing

software developed by the author reads the absorption data of CT slices stored in a binary form into 512x512 image matrices. The CT values of the matrix components are then converted into the saturation scale according to Eq. (2). Different built-in coloring schemes are also available for mapping the image matrices.

c. Foam Core flood Setup

The schematic of the foam core flood setup is presented in Fig. 1. It consists of a core holder in line with, on one end, a double effect piston displacement pump (Pharmacia Biothech P-500) in parallel with a gas mass flow controller (SIERRA) and, on the other end, a backpressure regulator set at 1.0 bar and a collector for the produced fluids. The gas mass-flow controller is used to ensure the supply of nitrogen gas (N_2) at a constant rate. The pump is used to inject the surfactant solution also at a constant rate. Four pressure ports along the core enable the monitoring of the local absolute pressures using transducers (ENRESS-HAUSER) and a personal computer equipped with a Kettley data acquisition system. All experiments are conducted in a thermostat room at 20 ± 1 C.

d. Core holder

The core holder is placed horizontally on the platform of the CT scanner apparatus and kept in place using a polymethyl methacrylate (PMMA) stand. The coreholder is made of polyether etherketone (PEEK), which combines good mechanical properties with a low X-ray attenuation. PEEK is also believed to transmit X-rays within a narrow energy window (refiltering the polyenergetic source X-rays), which appreciably minimizes the beam-hardening artifact due to the polychromaticity (sometimes called the interpetrous lucency artifact [Brooks et al., 1998]). This effect gives the appearance of dark streaks and flares in the vicinity of the boundary between the coreholder and the core (note that streaks can also be caused by aliasing [Millner et al., 1978]). The geometry and structure of the coreholder are also designed to minimize beam hardening and scattering artifacts in longitudinal imaging where the detected energy spectrum may vary with the projection direction. To eliminate the boundary flow effect at the inner surface of the coreholder, the core (diameter = 44 ± 1 mm and length = 180 ± 1 mm) is encapsulated in a thin layer of low X-ray attenuation Araldite (CW 2215) superglue, with CIBA HY 5160, Araldite CW 2215 as the hardener. During core mounting, the high viscosity of the superglue mixture ensures a very low penetration (less than 1.0 mm) of the core. The four pressure taps divides the core into three sections of 60, 40, and 80 mm: the sections are noted 1, 2, and 3, respectively.

2.2 X-ray CT-imaging settings

The fixed imaging settings for all foam core flood experiments are presented in Table 2. The X-ray tube of the CT-Scanner is operated at either 130 kV or 110 kV. The corresponding effective energies, at which a given material will exhibit the same attenuation coefficient as measured by the scanner, are typically about 50 to 60% of these values (see Refs. Millner et al., 1978; Alvarez and Macovski, 1976 for a practical procedure for determining the effective energy of a CT scanner). The use of low X-ray energy gives rise to the undesirable X-ray scattering effect. Moreover, because rock is high radio-dense, it is advisable to operate at the lowest energy and the highest ray density.

All CT images contain noise, that is pixel-to-pixel variations in the pixel value in the image of an object of uniform linear attenuation coefficient. It typically ranges from 3 to 20 HU. In the case of quasi-steady state foams in sandstones, the noise appears when subtracting two subsequent images of a fixed CT slice. Note that the quasi-steady state denotes the time-averaged foam behavior at pore scale. The noise therefore may include local fluctuations,

which cause detectable changes of the voxel compositions in time. It is also important to mention that the noise is proportional to the reciprocals of the squared X-ray tube current (mA), the scan time and the thickness of the CT slice. However, the longest scan time and the thickest CT slice are not always preferable, particularly in the imaging of dynamic processes such as transient foam and liquid displacements. A voxel is the three dimensional pixel, including the slice width. The average linear attenuation coefficient of the voxel thus reflects both resolution and partial volume effects.

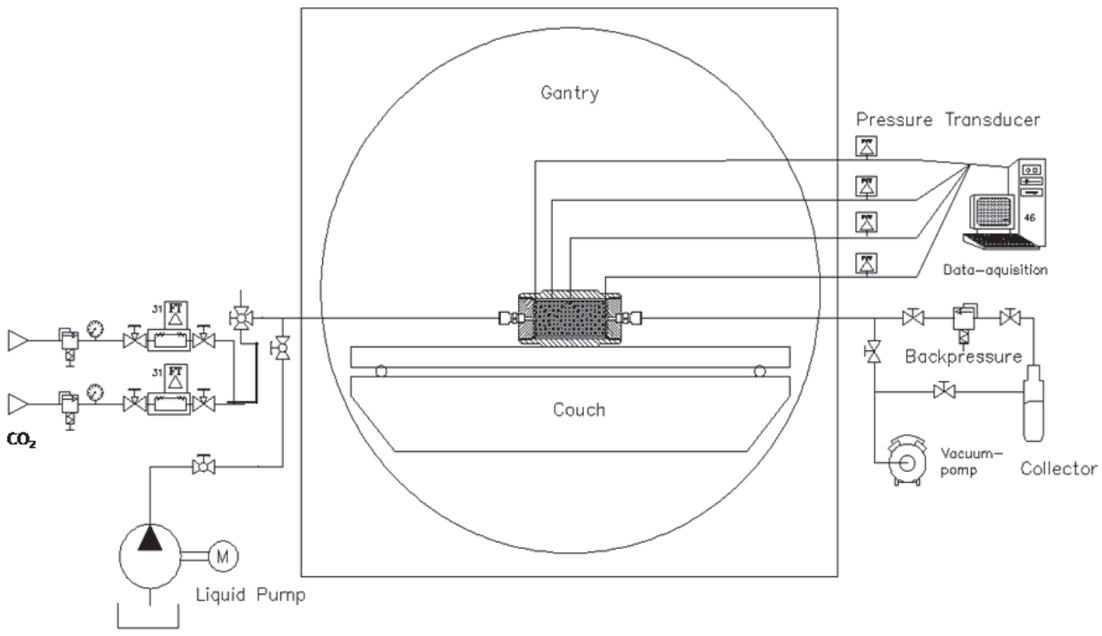

Fig. 1. The experimental setup used to investigate foam flow in porous media. Nitrogen (N_2) or Carbon Dioxide (CO_2) supplied via two dedicated mass flow controllers. CO_2 is used only for core saturation. Liquids (water or surfactant solution) are supplied using a precision piston displacement pump. Fluids are collected using a graded tube and gas counter. The core is placed with its axis in the flaming plane of the gantry of the X-ray tomograph, for the real-time visualization of rock features and in-situ foam induced fluid partitioning.

Specification	**Quantity**
Tube Voltage	110 kV
Tube curent	100 mA
Slice thickness	3 mm
Scan time	3 s
Field of View	160 mm
Image reconstruction kernel	Standard
Scan mode	Sequence
Couch feeding	6 mm span

Table 2. Imaging settings

2.3 Materials

Sandstone cores. Bentheim sandstone is used to carry out the experiments. This sandstone is macroscopically homogeneous according to its X-ray absorption data (for porosity and bulk density) and bulk X-ray diffraction data (for composition). The main physical properties of the Bentheim cores are presented in Table 3.

Permeability *(mD)*	Porosity *(%)*	Density *(g/ml)*	Main composition
1010	22.1	2.34	*Quartz*

Table 3. Properties of Bentheim sandstone

Gases. The analytical grade Nitrogen (N_2) and Xenon (Xe) are purchased from Scott High Pressure Technology. The qualities of these gases are presented in Table 4. We use these pure gases to make calibration gas mixtures of N_2 and Xe. For the foam core-flood experiments, a mixture of N_2 and Xe is used, and this mixture is also purchased from the Scott High Pressure Technology.

Quality	Xenon gas *(%)*	Nitrogen gas *(%)*
Xe	99.995	0.00
N_2	0.001	99.09
Ar	0.002	0.18
O_2	0.001	0.70
CO_2	0.000	0.04

Table 4. Qualities of bulk and tracer gas

2.4 Procedures

a. Core saturation

Since the X-ray absorption depends on the compositions of the attenuating system, the chemical properties of the Bentheim sandstone cores should be stabilized before carrying out the experiment. For this purpose, the Soxhlet method is used to extract native contaminants such as oil (using toluene) and other minerals (using a mixture of chloroform and methanol in distilled water). The core is then dried in a vacuum oven at 90 C. The initial saturation process starts with the injection of 200 pore volumes of brine (0.5 M *NaCl*) under vacuum (note that one pore volume is defined as the total volume of pore space of the core), and is followed with 200 pore volumes of surfactant solution at 1 bar backpressure to satisfy surfactant adsorption and ion exchange.

b. Fluid core-flood

Foam injection. The nitrogen gas and surfactant solution are co-injected directly into the saturated core at fixed rates. To investigate the fluid-rate effect on the displacement pattern in the Bentheim cores, three experiments with different total flow rates are conducted. An overview of fluid rates used is presented in Table 5.

The foam displacement process is visualized by constructing a series of 8 parallel images slicing vertically the core parallel to its axis. The central image is on the plane of the core axis (axis plane), whereas the other ones are placed two by two, symmetrically with respect to the axis plane. The spacing between two adjacent images (i.e., the couch feeding) is 4 mm.

Each five-image series is scanned in sequence from a couch position (CP) set to zero for the central image.

Foam types	Gas rate* (cm3/min)	Liquid rate (cm3/min)	Foam quality (%)
Foam-A	5.0	0.5	90.90
Foam-B	10.0	0.5	95.24

*Standard conditions

Table 5. Fluid rates used in the LDF experiments

Liquid injection following steady-state foam. Liquid is injected at a fixed rate after foam reaches full development. The first experiment is conducted with Foam-A, using a liquid rate of 2 cm^3/min. The effect of foam strength is investigated with Foam-B at the same post-foam liquid injection rate.

c. Determination of trapped gas based on a visual tracer method

The general principle of determining local foam mobility, using the X-ray CT technique and a tracer gas, is similar to that of visualizing gas-liquid displacement, as described in Section 2.1. However, some important differences are worth discussing. The mobility field of steady-state foam (native foam) in a porous medium can be identified through the visualized percolation of a tracer-foam, which is identical to the injected native foam, except for a small fraction of the tracer added to the bulk gas. To enhance the resolution of the mobility field, the tracer foam must have a significantly higher X-ray attenuation than the native foam. Having an atomic number of 54, Xenon gas possesses an attenuation coefficient much higher than nitrogen gas (atomic number of 7), thus is an ideal tracer.

It is important to note that the presence of the tracer should not cause a significant disturbance to the local equilibrium of the native foam, which is determined by two state-parameters of individual voxels: (1) phase saturation, and (2) average pressure. The former parameter is practically difficult to monitor during the transient displacement of the tracer foam since a detectable change in the X-ray attenuation reflects changes in both tracer concentration and phase saturation. The latter parameter is indirectly determined from the pressure drops measured over a large number of voxels along the main flow direction, which thus may not indicate precisely the fluctuation of the local pressure gradient due to foam trapping and remobilizing. However, intermittent foam trapping is an inherent feature of any quasi-steady state foam flow. Therefore, the fraction of the tracer foam, X_f, percolating through a single voxel containing the native foam can be determined through Eq. (3).

$$X_f(t,s,E_r) = \frac{HU_m - HU_{nf}}{HU_{tf} - HU_{nf}} \times 1000 \tag{3}$$

where HU_{nf} and HU_{tf} are the CT values of the native and tracer foams, respectively. Eq. (3) can be used to quantify exactly the fraction of mobile foam in the voxel, assuming a sharp compositional interface between the tracer foam and the native foam. However, the diffusion of Xenon across this interface and/or the instability of the foam films smear out the local tracer concentration profile (the mixing effect), thus leading to a poor interpretation

of the reconstructed compositional image. Fortunately, these effects can be minimized with highly stable foams, and by ensuring the dominance of convective over diffusive tracer transfers.

It is important to emphasize that foam trapping is a dynamic process. Gas trapping and remobilizing takes place at the pore scale, even in a macroscopic steady state foam process. This means that the propagation of the tracer foam observed in a CT slice reflects a local distribution of foam mobility. In this mobility field, trapped foam is defined as the lowest mobility (i.e. zero mobility and mobility of the same order of magnitude as the tracer diffusion rate in foam). Trapped foam also includes trapped and remobilized foam if this foam does not show a considerable net transport of the tracer in the main flow direction.

Selection of tracer concentration. The volume fraction of the tracer gas used should produce sufficient contrast between the native steady state and the injected tracer foams. It is thus necessary to quantify the sensitivity of the image resolution to the tracer concentration. For this purpose, the average CT values due to different tracer concentrations must be determined in both types of sandstones used. The procedure for the calibration measurement is as follows. First, the sandstone core must be cleaned and dried, as described in the core saturation procedure below. Three vertical longitudinal CT slices capturing most features of the entire core are selected for the sequence scanning: one slice on the plane of the core axis (central image) and the other two placed symmetrically with respect to the central image. The distance between two adjacent slices is 10 mm. An image series of the core without tracer gas is used as the reference for the image subtraction (see the core preparation procedure below). The imaging setting is presented in Table 2. Next, Xenon and nitrogen premixed to a chosen volumetric ratio are injected into the core where the system pressure is maintained at 1 bar (equal to the fixed core backpressure during foam flooding). The injection rate of the tracer mixture is 5 cm^3/min (standard conditions), fixed in all the calibration measurements. Note that the measured CT values of the individual voxels are in principle influenced by the voxel pressures because of the proportional relationship between the Hounsfield units and the tracer density. However, the injection gas rate used is chosen so that the ensuing pressure drop over the entire core is negligible with respect to the backpressure. This allows assuming a uniform density of gas throughout the core. The sequence scanning continues until the CT value of each image in series (obtained by averaging the CT values of its voxels) stays constant, signaling a full saturation of the tracer gas. The excess CT value due to the Xenon concentration is determined by subtracting the full-tracer-saturation images from the corresponding reference ones.

Tracer transport in dry cores. Without foam, the convection-dispersion of the tracer gas is mainly influenced by the topological disorder of the pore networks. However, with foam it is further modified by the local foam mobility and the effective tracer diffusivity due to liquid films. Therefore, the effect of pore-network heterogeneity on the tracer transport can be better distinguished in the absence of foam (dry cores). For this purpose, we conduct a tracer injection experiment on the Bentheim core. The procedure starts with the injection of 100 pore-volumes of nitrogen into the dry core at 1 bar backpressure. The injection rate is maintained at 3 cm^3/min (standard conditions). The tracer gas mixture with the tracer concentration being used for determining trapped foam is then injected at the same rate. Note that the use of a higher injection rate helps the convective from diffusive dispersion of the tracer. Moreover, it also causes a fast breakthrough of the tracer, thus limiting the number of image series needed to capture important features of the advancing compositional front.

Core recovery. To obtain the reproducibility of the data, the sandstone core of each type is recovered for use in a new experiment as follows. First, it is flushed with 200 pore volumes of distilled water in the presence of 40% ethanol. Taken out of the holder, it then undergoes a 24-hour-cleaning process to remove the remaining surfactant, using the Soxhlet extraction apparatus as described in Section 3.4 A. The cleaning solvent is a mixture of chloroform and methanol in distilled water. Finally, the core is dried in the vacuum oven at 100 C before going through the saturation process.

Tracer-Foam flood. Nitrogen foam is injected into the saturated core until reaching a steady state as indicated by (a) the sectional pressure drop profiles, and (b) the average CT values of the fluid system. The latter is determined from a set of seven parallel image planes with the same arrangement as that for the measurement of tracer transfer in the dry core above. The injection nitrogen is then switched to the tracer gas mixture, and the sequence scanning takes place every three minutes to produce successive image series of the transient tracer displacement. A full saturation of the tracer over the entire core is signaled by constant CT values of the images.

3. Results and discussion

3.1 Liquid displacement by foam (LDF)

Fig. 2 shows the CT images of the fluids during the liquid displacement by Foam-A (Q_g = 5 cm^3/min, Q_w = 0.5 cm^3/min) in a Bentheim core. Unless otherwise stated the images presented in this section are the central images (corresponding to CP = 0), which capture most of the features of the transient displacement. Note that the real elapsed time is presented in a dimensionless form (called dimensionless time, DT), defined as: tQ/PV, where t is the real time, Q is the total injection volumetric flow rate, and PV is the pore volume of the core.

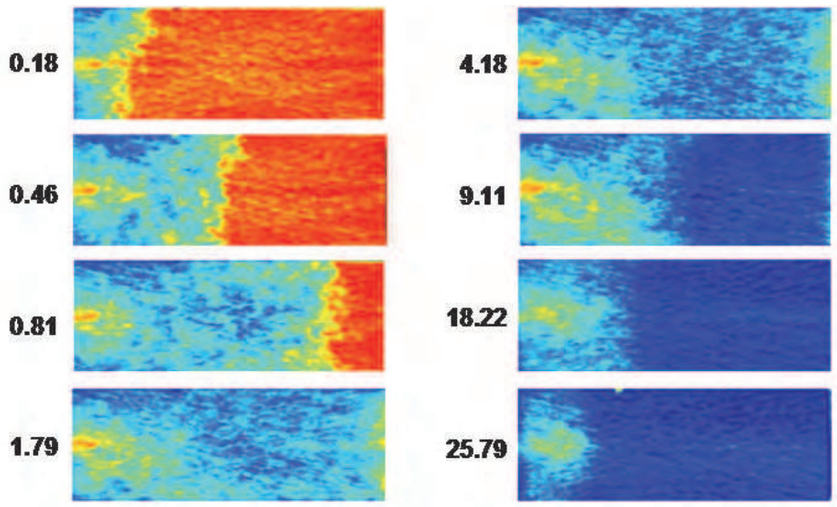

Fig. 2. The displacement by Foam-A (green/blue) in a Bentheim sandstone core, initially saturated with surfactant solution (red/yellow). Nitrogen and surfactant solution are directly co-injected at 5 (standard) cm^3/min and 0.5 cm^3/min, respectively. The images correspond to the centered longitudinal CT slice (CP = 0). First, a sharp foam front traverses throughout out the core after about 0.8 DT. After foam breakthrough, a second front develops and moves backwards to the inlet. Steady state is reached at about 25 DT.

Two foam displacement stages can be distinguished in the figure. The *first* stage runs from the beginning of the injection up to the breakthrough of foam at 1.79 DT. At first sight, the foam displaces the surfactant solution in a characteristic piston-like manner. However, a closer examination of the images reveals that we should consider three regions along the flow direction: (1) an upstream region characterized by a low liquid saturation, (2) a downstream region where liquid saturation is uniform and (3) a frontal region where a mixture of foam and free liquid gives rise to a fine fingering pattern. The *second* stage (indicated by the darkening of the blue region) starts after foam breakthrough and reaches maturity at 25.79 DT, corresponding to the establishment of the steady state flow regime. This stage is characterized by a strong secondary liquid desaturation (SLD), which initiates in the central portion of the core and propagates towards the inlet and the outlet. The well-known "capillary end" effect causing a relatively high liquid saturation near the core outlet is completely suppressed as the SLD drives through this region. However, this does not happen in the near-inlet region where the SLD could not exhaust a significant liquid-filled fraction.

To quantify the evolution of fluid saturations over the entire core, the CT data of five longitudinal image planes in each sequence scan are averaged in the transverse direction, resulting in one-dimensional liquid saturation profiles, as shown in Fig. 3. This figure shows more distinctly the two stages observed with the images in Fig. 2. Indeed, all profiles up to 0.81 DT, excepting the one at 0.11 DT, exhibit roughly the same trend: (1) a low (less than 55%) upstream liquid saturation, (2) a high (100%) downstream liquid saturation, and (3) a transition zone where the liquid saturation increases smooth, and rapidly towards the downstream.

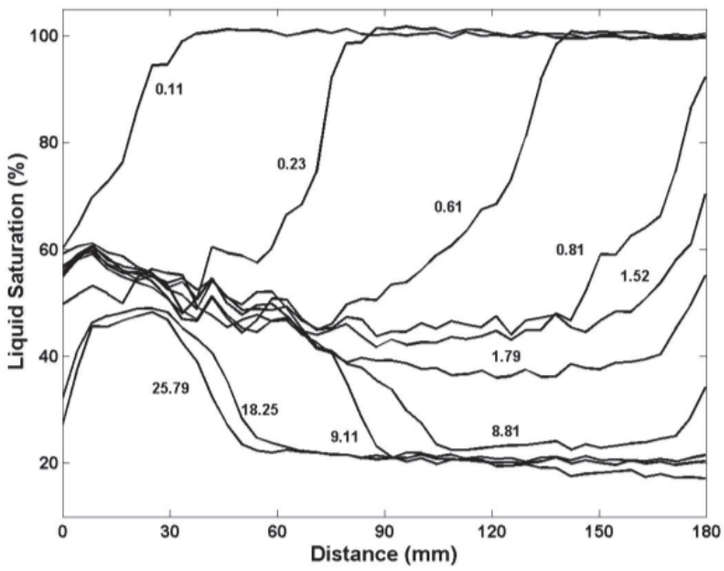

Fig. 3. Liquid saturation profiles (saturation versus distance from the inlet) at different times during the liquid displacement by Foam-A (Q_g = 5, Q_w = 0.5 cm^3/min).

The profile at 0.11 DT exhibits only a transition zone and the downstream saturation. Within the upstream region, the liquid saturation gradually declines from the inlet. For example, at

0.61 DT the saturation decreases by almost 10% from the inlet to the position 75 mm. Note that high capillary forces still retain a higher liquid saturation near the outlet at this time, which soon disappears as the second front propagates towards the inlet. However, the front does not approach the inlet at the steady state, leaving about 48% unswept liquid over 30 mm from the inlet.

Fig. 4 shows the pressure drops versus the dimensionless time for three different core sections (overall pressure drop over the core at the foam breakthrough is about 120 mbar). In the first and second sections, the pressure drops remain almost constant up to about 17 and 12 DT respectively, at which time the pressure in the third section reaches a steady value, corresponding to the time at which secondary liquid desaturation ceases in the third section. Then, the pressure drop in Section 2 increases. Similarly, the pressure drop in section 1 starts to increase as the pressure drop and the liquid saturation in Section 2 reach plateau values. The process of foam generation associated with liquid desaturation is self-amplifying as the former requires the local viscous pressure gradients to be sufficiently high, while, on the other hand, further foam generation leads to high local pressure gradients. Moreover, since gas expansion increases with the pressure drop induced by the steady state foam before liquid injection, it may contribute to foam/free liquid mobilization, and thus foam generation, especially far from the injection point.

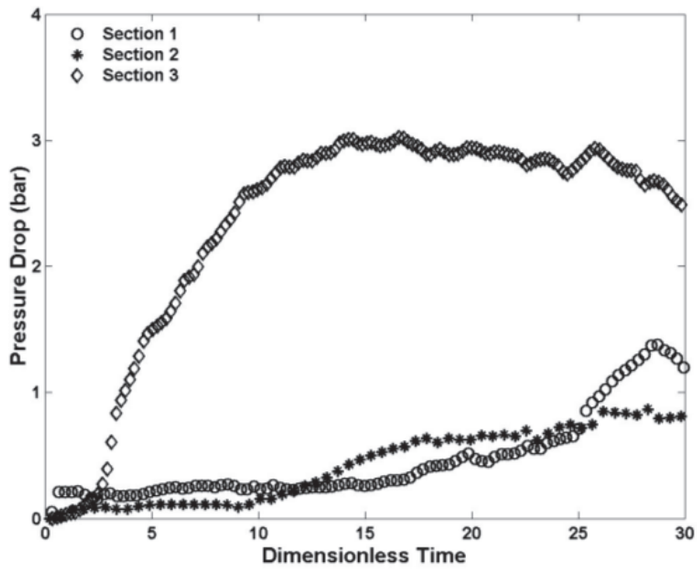

Fig. 4. Pressure drop histories of three successive sections during the liquid displacement by Foam-A (Q_g = 5, Q_w = 0.5 cm^3/min). No steady state is shown

However, liquid desaturation ceases as the capillary number reaches a critical value N_c^* (or the limiting capillary pressure P_c^*) defining the local equilibrium between foam generation and destruction. The capillary number, i.e. the ratio of viscous to capillary forces, has been commonly used to determine the relative importance of these forces on the mobilization of fluid in porous media. The capillary number can be expressed as

$$N_c \equiv |\nabla P| \frac{K}{\sigma_{gw}} \tag{4}$$

where ∇P is the local viscous pressure gradient. Note that several expressions have been used in the literature to express the ratio of viscous and capillary forces [Gauglitz et al., 2002; Tanzil et al., 2002; Fulcher et al., 1985], but they have the same generic meaning as Eq. (2). The concept of critical capillary number explains the above observation that the quasi-steady state is obtained, for instance in Section 3, regardless of the substantial foam development in the preceding section. The liquid saturation corresponding to N_c^* is not necessarily the irreducible saturation (that is mainly determined by rock properties). Hence, if the system reaches an irreducible saturation state, foam may develop (indicated by increasing pressure drop) without necessarily a change of the liquid saturation as observed in some previous studies [Kovscek and Radke, 1994; Osterloh and Jante, 1992]. We believe that in this particular regime, mobilization and division of stationary foam will play an important role in foam generation.

3.2 Effect of fluid rate on LDF

For given properties of a porous medium, one way to increase the capillary number consists of increasing the interstitial fluid velocities. Although the latter is mainly determined by the local foam mobility, we assume that it increases with the superficial (injection) fluid velocities. For the sake of comparison, first consider the case where Q_w is the same as used for the previous Foam-A, and Q_g is increased by a factor of two (= 10 cm^3/min, Foam-B in Table 5). The displacement of liquid is shown in Fig. 5. The first discernible difference from Foam-A is the gravity effect on the traveling foam front, as foam first breaks through in the upper part of the core (see image at 0.70).

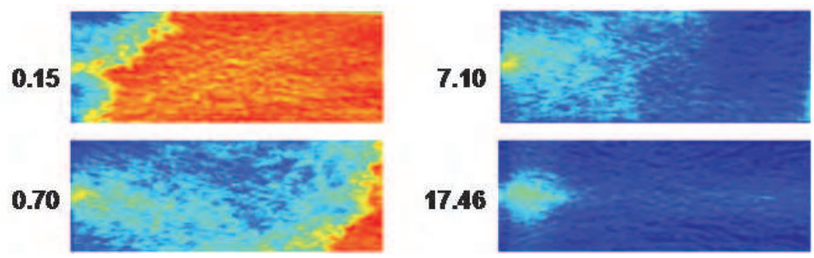

Fig. 5. The displacement by Foam-B (green/blue) in a Bentheim sandstone core, initially saturated with surfactant solution (red/yellow). Nitrogen and surfactant solution are directly co-injected at 10 (standard) cm^3/min and 0.5 cm^3/min, respectively. The images correspond to the centered longitudinal CT slice (CP = 0).

The gravity override is normally suppressed when foam in the frontal region develops strongly enough to raise the relative importance of viscous to bouyancy forces. However, this is not observed with Foam-B, possibly due to the fact that the high gas rate in Foam-B might be unfavorable for foam generation, particularly in Section 1. Additionally, gas saturation in this section for Foam-B is somewhat higher than that for Foam-A, resulting in a relatively higher bouyancy force.

The gravity effect leads to an earlier emergence of the SLD as compared with Foam-A. This is illustrated with the liquid saturation profiles shown in Fig. 6. Similar to Foam-A, the evolution of liquid saturation is composed of two distinct stages, except that, in the first stage, the elevated gas rate results in a rather uniform liquid saturation within the upstream region, and reduces somewhat the "entrance" effect. The sharp decrease in liquid saturation

visible in the first few millimeters near the inlet is consistent with the desaturation in the corners as observed in the images (see Fig. 5). Additionally, the second liquid-saturation front propagates towards the inlet distinctly faster than that of Foam-A (comparing the profiles at 9.11 and 38 DT in Figs. 3 and 6, respectively), and approaches closer to the inlet. Foam still does not propagate as strongly in the near-inlet region as it does further downstream, even though injection gas rate is higher by a factor of 2. This suggests that foam generation is less dependent on the gas rate. In fact, comparing the pressure drop profiles of Foam-A and B shown in Figs. 5 and 7, respectively, the pressure drop over the first section at 30 DT is roughly 1.20 bar for Foam-A, which is slightly higher than that for Foam-B (about 0.90 bar).

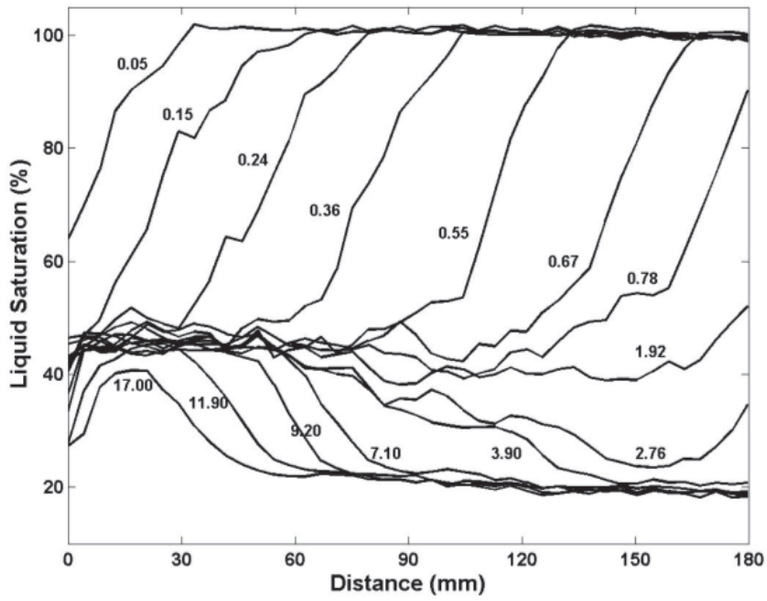

Fig. 6. Liquid saturation profiles (saturation versus distance from the inlet) at different times during the liquid displacement by Foam-B (Q_g = 10, Q_w = 0.5 cm^3/min).

3.3 Foam displacement by liquid (FDL)

Fig. 8 shows a set of images (CP = 0, +8, +16) of the fluid partitioning during the injection of the surfactant solution (at 2 cm3/min) in the Bentheim core. At 3 DT, the images show that the liquid flows according to a characteristic finger pattern. This flow structure may be ascribed to the non-uniform foam mobilization by the injected liquid. The size and shape of the finger seem to be controlled by two effects. The first is the compressibility of foam and the second is the "wetting film" flow through the space occupied by the stationary foam (i.e. liquid flows preferentially in the wetting film). In particular, the downward bending of the liquid finger, in the midst of the trapped and expanding foams, is due to the gravity effect. Liquid saturation is approximately 82.0% within the finger, while in the surrounding foam region it remains at about 22.3%. The former indicates about 30% of gas probably trapped within the network of percolating liquid. Considering images taken at successive times (e.g. CP = +8, at 1.75, 3.0, and 6.0 DT), it can be seen that the liquid content of the finger increases in time, corresponding to the diminishing of the isolated gas blobs, as the correlation length

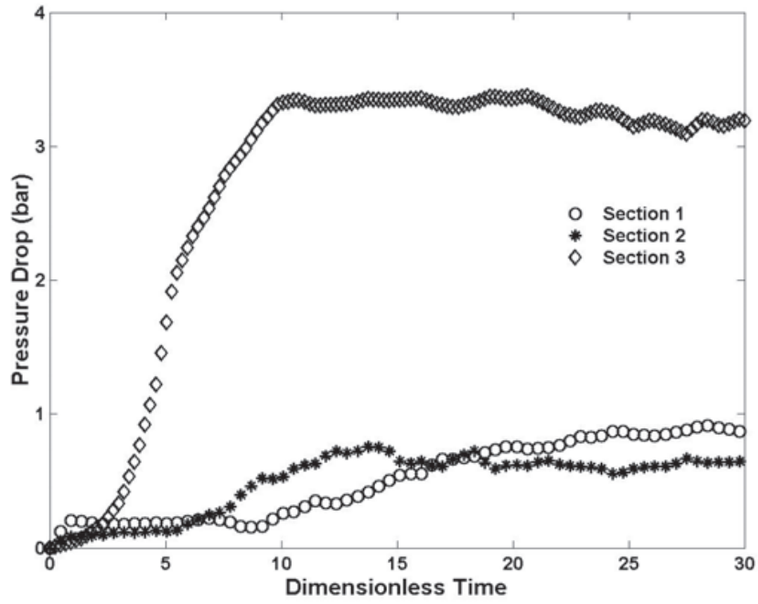

Fig. 7. Pressure drop histories of three successive sections during the liquid displacement by Foam-B (Q_g = 10, Q_w = 0.5 cm^3/min). Steady state is shown.

of the liquid network is refined. Moreover, the finger grows from the beginning of the injection of liquid until it breaks through. It is thicker near the inlet, but becomes thinner as the distance from the inlet increases. The lateral development of the finger near the inlet can be explained by the fact that foam developed much more strongly towards the outlet during the foam injection (see Fig. 2), and that the invasion energy of liquid is dissipated due to the viscous flow. In addition, the inherent gas expansion tends to reduce foam density more near the inlet than in the downstream region (because of no foam injection and one-dimensional flow). As a result, the probability of a foam-filled pore being invaded by liquid is higher towards the inlet.

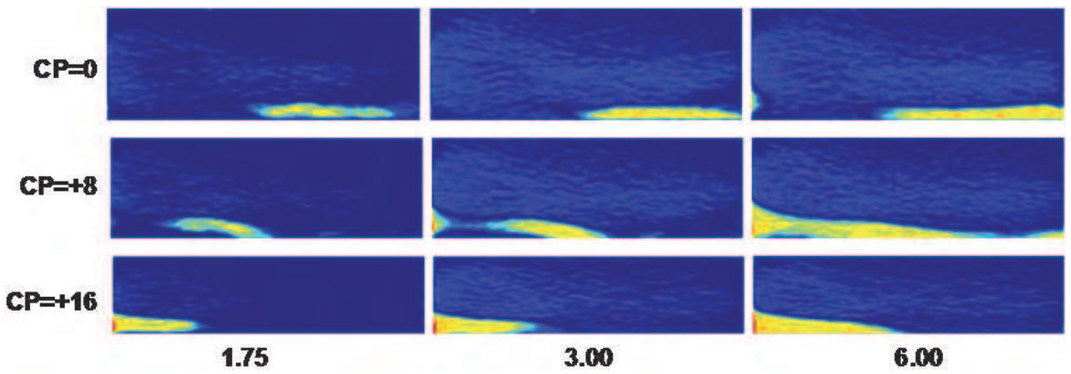

Fig. 8. Macroscopic pattern of fluid partitioning during the FDL process. Liquid fingering emerges after the injection of surfactant solution, following the steady state Foam-A in the Bentheim core (see Fig. 2). The liquid finger has an asymmetrical structure spanning over three image planes (CP= 0, +8, +16).

The pressure drops corresponding to the above images are shown in Fig. 9. The pressure drops over Sections 1 and 2 are added because the former is extremely low. In both core sections (1+2 and 3), the pressure drop evolves in three regimes. In the first regime (from 0 to about 1.2 DT), the pressure drop first increases and then falls sharply. Reporting similar pressure drop profiles, Cheng and co-workers [2001] attributed the brief increase in the pressure drop to the fact that the liquid rate is higher than the actual foam rate in the core, (near the inlet). To be more precise, in the range of flow rates used, this can actually be due to the compression of the small volume before the inlet core surface, where the gas and the surfactant solution were mixed during foam injection. In the second regime (1.2 to 5.5 DT), the pressure drop declines gradually, consistent with the "wetting film" flow and the development of the finger, as discussed above. Gas expansion also contributes considerably to the pressure decline. Finally, in the third regime, which runs from 5.5 to over 40 DT (only data up to 7 DT are shown in Fig. 9), a quasi-steady state flow has been is established. Foam remains trapped in the porous medium, since no gas production was observed during this time. The liquid finger also reaches an apparent stability in this regime.

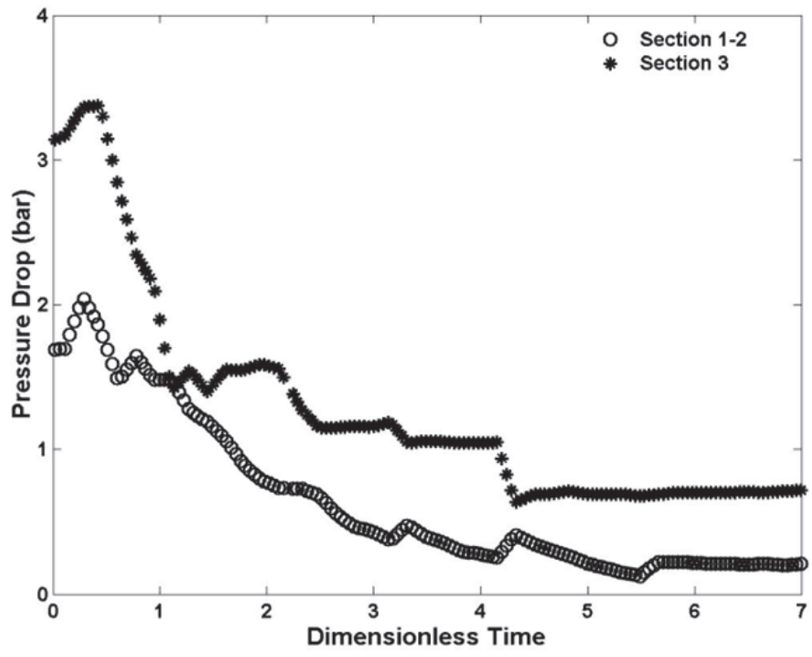

Fig. 9. Pressure drop histories of Section 1 Plus 2 and Section 3 during the injection of surfactant solution at 2 cm3/min, following the steady state Foam-A in the Bentheim core (Fig. 2).

3.4 Effect of the initial steady-state-foam strength on FDL

Fig. 10 shows the development of the liquid finger at 1.22 and 3.00 DT, during the injection of surfactant solution (at 2 cm^3/min) following Foam-B (see Fig. 5 for the foam injection stage). Note that - for the sake of comparison on the same time scale, the definition of the dimensionless time is the same, except that the total injection flow rate Q is fixed at 1 cm^3/min (even for the actual injection rate of 2 cm^3/min).

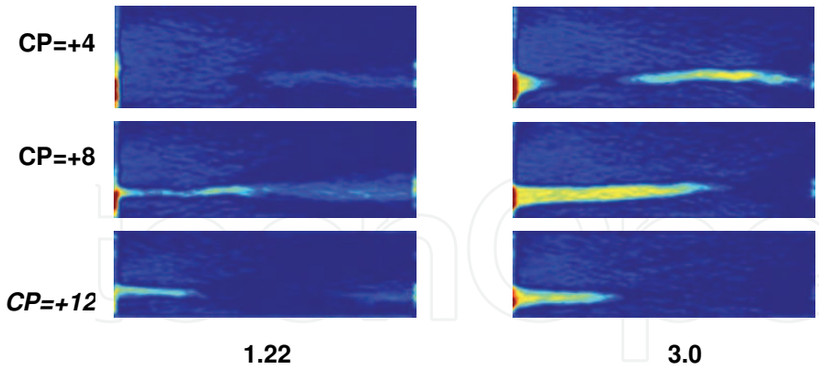

Fig. 10. Macroscopic pattern of fluid partitioning during the FDL process. Liquid fingering emerges after the injection of surfactant solution, following the steady state Foam-B in the Bentheim core (see Fig. 5). The liquid finger has an asymmetrical structure spanning over three image planes (CP= +4, +8, +12).

Unlike Foam-A (see Fig. 8), Foam-B reduces greatly the tortuosity of liquid percolation as the finger is confined only within the CT slices from CP = 4 to +12, (instead of 0 to +16 for Foam-A). Additionally, the finger lies away from the boundary of the core and gradually grows upwards along the core axis, indicating the decreasing gravity effect. This is because Foam-B is somewhat stronger than Foam-A, as indicated by the corresponding pressure drops during the foam injection in Figs. 4 and 7.

The image CP = +8 at 1.22 DT exhibits a distinct contrast in density of the percolating liquid network: high (low) in the first (second) half-length of the core (image CP = +8). More importantly, within the low liquid-density region, the finger grows into the image plane CP = +4 at the expense of the part in image CP = +8 at 3.00 DT. This provides an insight into the percolation pattern of liquid controlled by foam mobilization and gas expansion. Qualitatively, after driving "easy-to-mobilize" foam out of a certain pore fraction, the percolating liquid may then encounter "difficult-to-mobilize" foam, which leads to a buildup of the local liquid pressure. Once (a portion of) this foam is mobilized, the liquid pressure decreases as a result, causing a temporary increase in the local pressure gradients around the liquid-invaded region. The latter promotes the gas expansion, especially when the pressure energy of the foam domain is sufficiently high. This mechanism is most likely responsible for the simultaneous growth and decay of the liquid finger. It also implies that when the gas expansion becomes insignificant, the finger simply grows by virtue of foam mobilization, thus reaching a stable structure as observed in the images at 3.00 DT. The average liquid saturations within the stable finger and over the entire core at this time (roughly 77.1 and 26.7%, respectively) are a bit lower than in Foam-A (roughly 82.0 and 29.8%, respectively), consistent with a relatively stronger Foam-B.

3.5 Effect of liquid rate on FDL

One might expect that a decrease in liquid rate could results in a "weaker" liquid fingering, or on the other hand a clarifying of the picture of the "wetting film" flow regime. Let us clarify this with the result of Foam-B displacement at a lower liquid rate (1cm^3/min), as shown in Fig. 11. The images in this figure show a mature liquid finger at 4.25 DT, which

initiates in both CT slices CP = - 8 and - 12 and then grows mainly into the latter slice before coming back in the former slice.

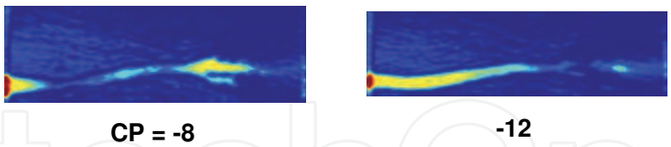

Fig. 11. Macroscopic pattern of fluid partitioning during the FDL process. Liquid fingering emerges after the injection of surfactant solution at 1 cm3/min, following the steady state Foam-B in the Bentheim core (see Fig. 5). Images are taken at 4.25 DT.

Compared with the case of 2-cm^3/min-liquid rate in Fig. 10, the first important difference is that the finger is now situated in the opposite side of the central image plane, as indicated by the native CP values. The only difference between these two experiments is the liquid injection rate. This implies that the position of the finger is not just determined by the properties of the medium, but also by the flow properties. In particular, lowering the liquid rate leads to a "delay" between the liquid invasion and gas expansion processes, and, as discussed previously, the latter strongly influences the evolution of the percolating liquid network. In fact, the finger obtains a smaller size as the liquid rate is decreased (comparing the finger structures in Figs. 10 and 11). Remarkably, its high-liquid-density-region does not approach the outlet as observed with the previous foams, suggesting the emergence of the "wetting film" flow regime in the subsequent region. In this regime, the initial liquid saturation is of the order of liquid saturation induced by the previous foam flow, and does not change significantly during the liquid percolation. As a result, the displacement of foam by liquid is constrained by the effective foam yield stress. Although the Bentheim core is macroscopically homogeneous, the finger "tip" is still branching. Therefore, the apparent discontinuity of the liquid saturation across the branching finger "tip" may stand as proof of a transition from "pore-scale, piston-like displacement" to "wetting film" flow regime. Furthermore, one can expect that an increase in the liquid rate may counteract the gravity force throughout the foam bank. This can be seen through comparing the mature finger structures in Figs. 10 and 11.

3.6 Calibration of contrast enhancement using Xenon for gas trapping measurement

Fig. 12 shows CT enhancement as a linear function of the Xenon concentration in the Bentheim core. The discrete data points designate the steady state CT values of the flowing tracer gas averaged over three CT slices. The pressure drop across the core is 0.8 ± 0.2 mbar, which is much smaller than the backpressure (1 bar). Note that for the tracer concentrations used we found the steady-state CT values to be insensitive to the variation of the injection rate over a rather wide range from 2 to 15 cm^3/min (standard conditions). The slope of the fitting line in Fig. 12 gives a contrast enhancement of 0.68 HU per added percentage of the Xenon gas. This value reflects the bulk density and the composition of the Bentheim sandstone used. As shown later, the overall pressure drop induced by steady state foams is roughly 8 for the Bentheim core. Therefore, for a given Xenon concentration, the CT contrasts of the Xenon gas shown in Fig. 12 will be slightly enhanced as the tracer density increases with the system pressure.

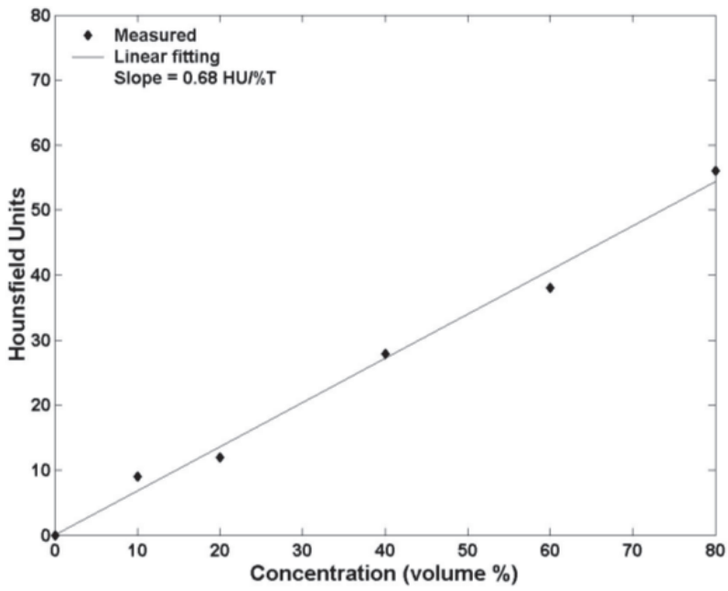

Fig. 12. The incremental CT value (HU) as a linear function of Xenon concentration for Bentheim core. The discrete data indicate the CT value of the tracer mixture flowing steadily in the cores at 1 bar backpressure, determined from averaging CT values over 3 image planes CP=-10, 0, and +10. The slopes of the linear fitting lines show increments of 0.68 due to one additional volume percentage of the tracer in the Bentheim core.

However, the use of very high tracer concentration is not recommended since it might lead to a substantial difference in the rheological properties between the native and tracer foams. We thus chose to use a mixture of 25% Xe in all trapped gas measurements. In tests of Xenon up to 40% for 90%-quality foam for both types of sandstones, we have found an insignificant change in the steady state overall pressure drops, suggesting a minimum disturbance of the tracer foam to the local fluid mobilities. It is worth mentioning that, by scaling the tracer foam saturation according to Eq. (3), the effect of the voxel-to-voxel variations in pressure due to foam is localized and averaged out. Additionally, the noise found in the CT images of steady state nitrogen foams normally ranges from zero to 12 HU. Since the image pixel's size is normally fixed for a fixed CT field of view, larger CT slice-width can be used to increase the total mass of the tracer per voxel, thus improving the signal-to-noise ratio, especially for a relatively high average fraction of quasi-stationary foam per voxel.

3.7 Tracer transport in dry Bentheim core

Fig. 13 shows the percolation of the tracer (green/red) in the Bentheim core after 501 and 1134 second injections of the tracer mixture. Only images CP = 0 and +12 are shown since they capture most of the features of the transient displacement of nitrogen by the tracer. The steady state pressure drop over the core is 0.5 ± 0.2 mbar, resulting in quasi-isobaric CT values of the voxels. The four-second delay between two adjacent images does not seem to cause a discernable shift of the advancing apparent tracer fronts over the image planes. The lateral distribution of the tracer concentration is rather uniform, confirming the macroscopic homogeneity of the Bentheim sandstone core. The longitudinal dispersion of the tracer is remarkably demonstrated by a 'hairy' pattern of the tracer concentration distribution in the main flow direction.

Consider a typical core section denoted by the white rectangle in the images CP = 0 in Fig. 13. Although the tracer first broke through this section after 501 seconds, its concentration continues increasing afterwards, indicating a wide distribution of the pore-scale travel times of the tracer molecules. Particularly, in the image CP = 0 at 1134 seconds, the tracer concentration around the core axis near the inlet is lower than in the surrounding radial region, even though the images in Fig. 13 show that there is uniform distribution of the tracer in the volume before the core inlet.

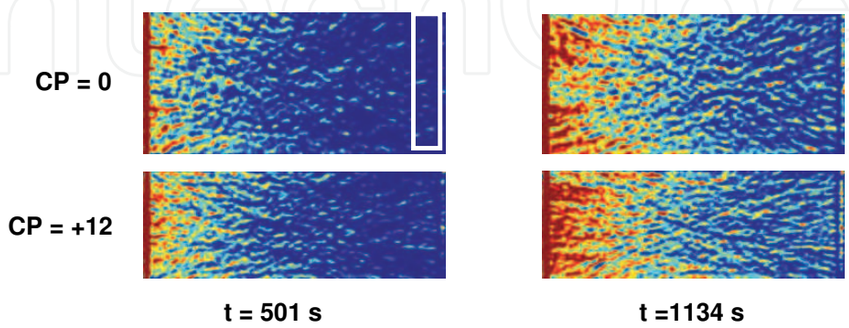

Fig. 13. Propagation of the tracer gas mixture with 25 vol.% Xe in the Bentheim core, following steady state nitrogen flow at 1 bar backpressure. The injection rate of 3 cm^3/min (standard conditions) is applied equally for both Nitrogen and tracer mixture. The white rectangles show the non-uniform advancement of the tracer saturations in flow direction due to the significant tracer dispersion. Distribution of tracer concentration is rather uniform in the transverse direction.

Since the longitudinal dispersion of the tracer is relatively dominant for this Bentheim core, the magnitude of tracer dispersivity can be evaluated through one-dimensional tracer saturation profiles (S_T) at different points in time, plotted versus positions along the core as shown in Fig. 14. The saturation value at each position is determined by averaging the voxel tracer saturations over the corresponding cross sections of the seven CT slices. Examine first the 91s-profile in Fig. 14. The tracer percolates almost one-third of the total core length, while it displaces roughly just 35% of the native nitrogen gas near the inlet region. Comparing with the images in Fig. 13, this is due to the significant dispersion effect. This effect is observed more obviously in the subsequent profiles. The typical 501s-profile exhibits three distinct saturation regions: (1) the near inlet region with $S_T \approx 100\%$, (2) the transition region with an abrupt fall of S_T from 100 to roughly 50%, and (3) the relatively largest region with a further gradual decrease of S_T to slightly above 22%. Obviously, the tracer transport is mainly governed by convection in the first region, whereas the last region is characterized by convection and dispersion.

3.8 Foam tracer transport in a horizontal Bentheim core

Fig. 15 shows the displacement of the steady state mobile nitrogen Foam-A by Tracer-Foam-A. Both foams have the same quality of 90.90% with the liquid and (standard) gas rates of 0.5 and 5 cm^3/min, respectively. The pressure gradient of 0.54 ± 0.03 bar/cm in Foam-A remained almost constant during the tracer foam injection. The five image planes in Fig. 15 show a three-dimensional structure of the relatively high mobility foam region. The images on the plane CP = 0 resemble its neighboring planes CP = ± 6 (not shown). Consider the first

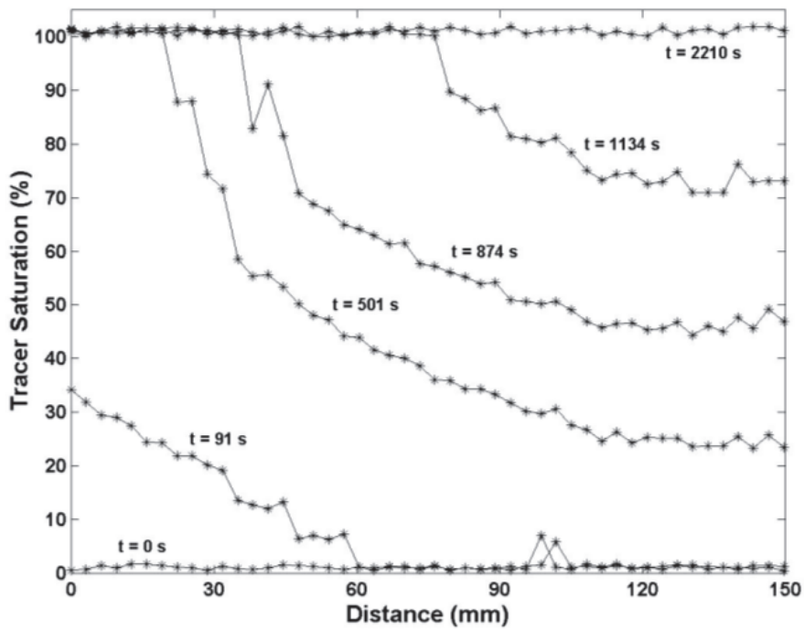

Fig. 14. One-dimensional tracer concentration profile plotted versus distance from the inlet, during the injection of the tracer mixture in the Bentheim core (see Fig. 13). The tracer saturation at each position along the core is determined from averaging the corresponding tracer saturations of individual voxels in the transverse direction over the three CT slices CP =-12, 0, and +12.

Image series in Fig. 15 taken after 990 seconds injection of Tracer-Foam A. The tracer penetrates, about 10 mm deep into the core, uniformly over the cross-sectional area. Further downstream, it propagates preferentially in the upper half of the cylindrical core, and apparently has broken through at the outlet by this time. The most mobile foam forms a cap at the top of the core growing laterally from the upper circumference of the core. A further development of this cap shown in the subsequent 1590-seconds-image series suggests an increase in the spreading of the tracer saturation with the gradually growing cap size. The tracer-saturation spreading reflects the degree of the dispersion effect on the tracer transfer within the cap, while the gradual growth of the cap indicates the diffusion rate of the tracer from the high mobility foam into the surrounding liquid and the quasi-stationary foam. It has been established that the foam films impose significant resistance to the tracer diffusion process. Therefore, for a sufficiently high interstitial velocity of foam, we expect the macroscopic structure of the high mobility foam region to become stably distinct soon after breakthrough of the tracer. This is confirmed in Fig. 15 where the tracer exhibits its stable profile at 2116 seconds. The cap size is well established while the spreading of tracer saturation within the cap is still evolving. Particularly, examining the three images CP = 0 reveals that the tracer near the inlet region around the core center percolates much slower than at the top of the cap. This suggests that the cap contains almost mobile foam. A large remaining fraction of foam is thus either stationary or has a very low mobility relative to that of foam in the cap.

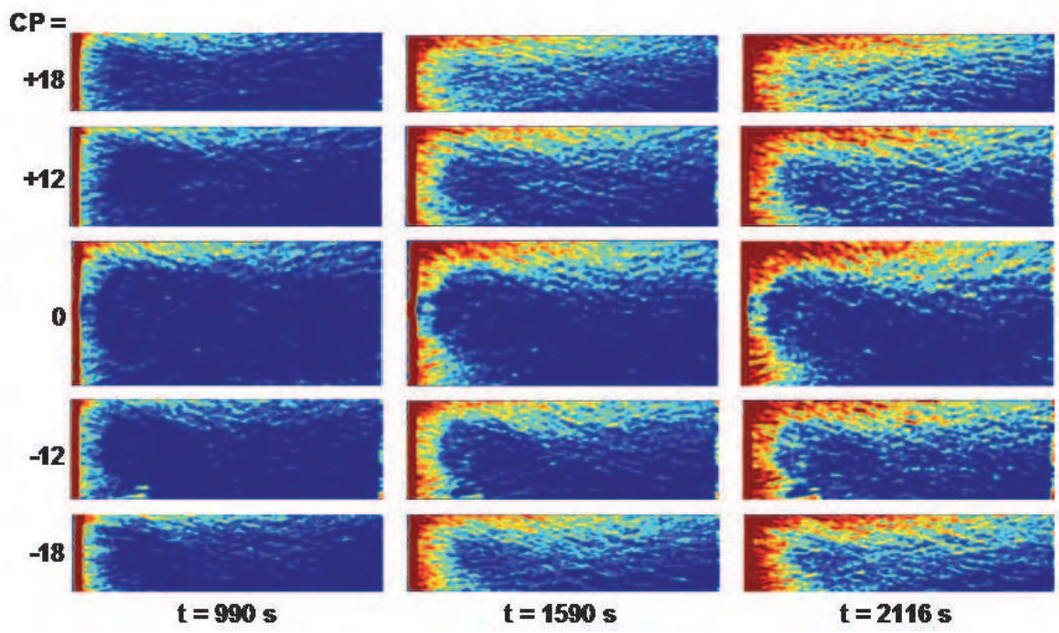

Fig. 15. Displacement of steady state nitrogen Foam-A by the tracer foam in the horizontal Bentheim core. Both foams have the same quality of 90.9% with (standard) gas and liquid rate rates of 5 and 0.5 cm^3/min. Tracer concentrations (red/green) reflect the mobile foam, forming a cap-shaped structure in the upper half part of the core. The tracer foam saturation is highly dispersed within the cap. The remaining region (blue) exhibits the quasi-stationary foam.

Fig. 16a presents the corresponding one-dimensional tracer saturation (S_f) profiles, determined by the same averaging method as used for the dry case above. The profile at 990 seconds shows two distinct saturation regions. In the first region (region 1), from the inlet to around 30 mm downstream, the tracer saturation (S_f^1) falls from 40% to slightly above 10%. In the remainder of the core (region 2), tracer saturation (S_f^2) is quite uniform around 10% up to 110 mm, and then decreases gradually to about 8% near the core outlet. Subsequently, the slope of the tracer saturation profile in the main flow direction remains almost the same, but the rate of increase of saturation at a fixed position slows down after about 1500 seconds. This is demonstrated in Fig. 16b, where tracer saturation averaged over the cross-section at the middle position of the core is plotted versus time. The rate of change of saturation in at this position is significantly reduced after roughly 2116 seconds. The images in Fig. 15 show that the significant increase of S_f up to 1590 seconds reflects the fraction of highly mobile native foams displaced by the tracer foam in the cap. The short invasion of the tracer foam in the lower part of the core can result from the intermittent trapping and remobilizing of foam near the inlet region associated with the tracer diffusion. This particular transport phenomenon, that is analogous to the convection-diffusion of the tracer in the fraction of very low mobility foams within the cap, explains the uniform gradual increase of S_f as observed after 1590 seconds. Since the one-dimensional distribution of trapped foam fractions S_t equals to $(100 - S_f)$, the selection of any S_f profile far before 1590 seconds can lead to the overestimating of trapped foam due to a fraction of low mobility native foams, which have not yet been displaced by the tracer foam. The profiles far after

this time, on the other hand, can underestimate trapped foam due to the tracer diffusion. Therefore, a good estimate of trapped foam (or quasi-stationary foam) can be obtained at the time where the rate of increase of saturations along the core slows down. In this sense, according to Fig. 16b we chose the profile at 2116 seconds, and found the average quasi-stationary foam fractions of 58 ($\overline{S}_t^1$) and 77% ($\overline{S}_t^2$) in regions 1 and 2, respectively. Note that $\overline{S}_t^1$ and $\overline{S}_t^2$ are used instead of an average of trapped foam $\overline{S}_t$ over the entire core only to emphasize the fluctuation of gas trapping near the inlet, particularly in the lower part of the core as discussed above. The best estimate of the trapped gas fraction under the given flow conditions is $\overline{S}_t^2$ =77%.

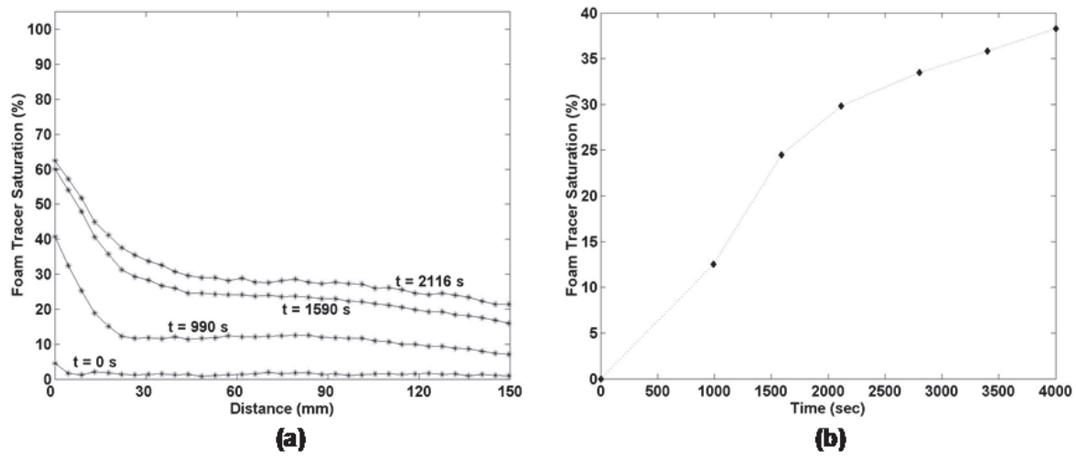

Fig. 16. Cross-section averaged tracer saturation during the displacement of the nitrogen Foam-A in the Bentheim core: (a) One-dimensional foam-tracer saturation profile plotted versus distance from the inlet, (b) The tracer saturation at the middle position of the core (75 mm from the inlet) plotted versus time. This figure shows that the rate of increase of tracer saturation is significantly reduced after 2116 seconds, indicating most of highly mobile native foam being displaced by the tracer foam.

3.9 Effect of gas rate on foam tracer transport in a horizontal Bentheim core

Consider Foam-B with 95.24% quality, having the injection (standard) gas rate twice that in Foam-A and the same liquid rate. The displacement of the steady state Foam-B by Tracer-Foam-B is shown in Fig. 17 at three different points in time. The structure of the high mobility foam cap is similar to that observed with Foam-A (Fig. 15), except that part of it in the image CP = 0 tends to grow away from the upper core circumference. This trend becomes more obvious after 976 seconds, as shown by the last two images series in Fig. 17. Particularly, a small finite cluster of the high tracer saturation propagates slowly in the lower half of the core in images CP = -6. It is possible that it originates from a small percolating cluster of mobile foam near the inlet, which is then somehow trapped. The diffusion process can thus be responsible for the subsequent growth of this cluster. More remarkably, the boundary between the high mobility foam cap and the surrounding region is much sharper than in Tracer Foam-A (see Fig. 15), and does not change significantly in structure and size even after the tracer breakthrough. Furthermore, the high tracer saturation within the cap propagates steadily and faster according to the recorded elapsed

times in Fig. 15 and 17. More than likely this results from the increase in the injection gas rate, and the ensuing modification of foam rheology through rate-dependent mobility [Kovscek and Radke, 1994; Alvarez, 1996; Osterloh and Jante, 1992]. In our experiments above, doubling gas rate resulted in the steady state pressure gradient of 0.72 ± 0.03 bar/cm, slightly higher than that in Foam-A (0.54 ± 0.03 bar/cm), suggesting a shear thinning-like foam behavior. This will increase the relative dominance of the convection over diffusion of the tracer, which helps estimate more precisely the actual trapped foam fraction.

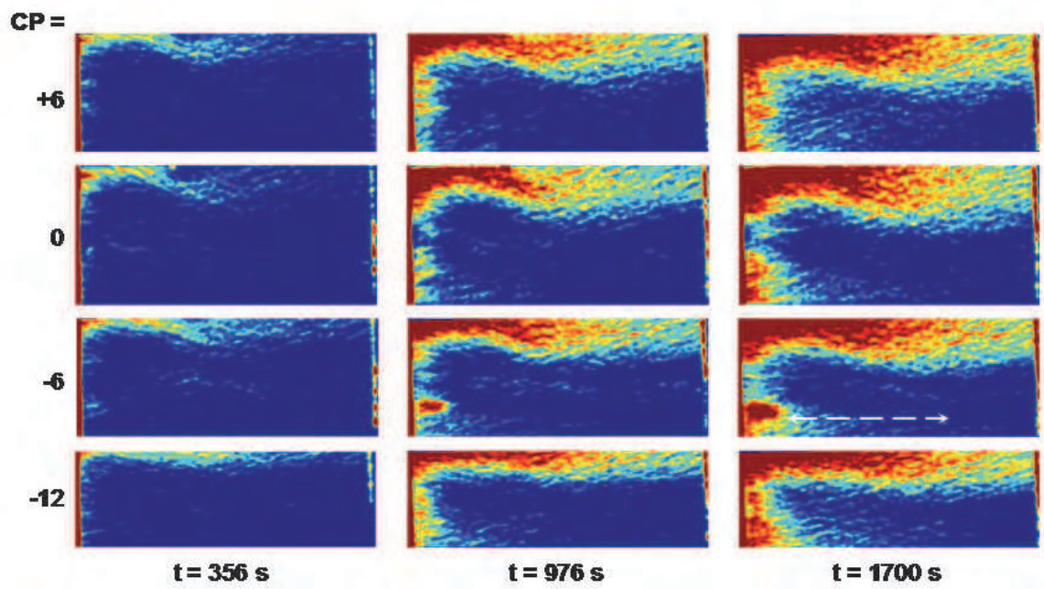

Fig. 17. Displacement of steady state nitrogen Foam-B by the tracer foam. Both foams have the same quality of 95.24% with (standard) gas and liquid rate rates of 10 and 0.5 cm^3/min. The highly mobile foam (red/green) concentrates in the half upper part of the core. A small cluster of tracer foam in the lower part of the core near the inlet reflects most likely the fluctuation of gas trapping. The remaining region (blue) exhibits the quasi-stationary foam.

Consistently, the rate of increase of tracer saturations in Foam-B along the core is higher than for Foam-A as shown in Fig. 18, while the shapes of tracer saturation profiles due to both foams are very much similar. A closer examination of the saturation differences between two adjacent profiles reveals that the maximum difference apparently advances downstream in time. This most likely corresponds to the advancement of high tracer saturations in the high mobility foam cap as observed in Fig. 17 (red color). In particular, the profiles at 1700 and 2300 seconds are very close up to around 80 mm from the inlet, and then diverge gradually towards the outlet. The former indicates a rather complete displacement of most of mobile native foams in this region at about 1700 seconds, while the latter reflects the continuous displacement of the low mobility native foams up to 2300 seconds. Note that Fig. 18 does not show the profiles after this time since the subsequent tracer saturations along core changed uniformly and very slowly. Therefore, for the reasons previously mentioned in the section 31.3 A (on Foam-A), we used this profile to determine the average fractions of quasi-stationary foam for regions 1 and 2, which gives $\overline{S}_t^1$ = 45 and $\overline{S}_t^2$ =65%.

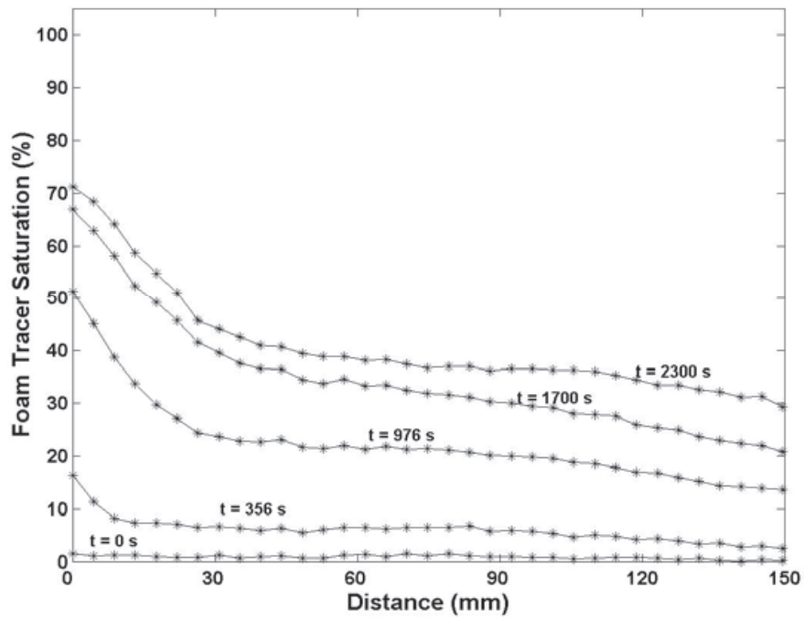

Fig. 18. One-dimensional foam-tracer saturation profile plotted versus distance from the inlet, during the displacement of the nitrogen Foam-B in the Bentheim core (see Fig. 17). The maximum difference in saturation between two adjacent profiles advances towards the outlet, indicating the propagation of the high tracer saturation front.

Notwithstanding a substantial difference in gas rate, the three foams above exhibit a similar macroscopic pattern of quasi-stationary foam. Due to the high foam qualities used, we surmise that the limiting capillary pressure (P_c^*) governs the "shear thinning" rheology of foam as observed in these cases [Khatib et al., 1988; Rossen and Zhou, 1995]. In this regime, foam texture self-regulates to maintain P_c^*. For instance, foam coalescence increases in response to the elevated gas rate. The experimental results suggested a decrease of P_c^* with increasing gas rate. We attribute this to the fact that the instability of foam at high gas rate affects primarily the mobility of flowing foams through the mechanical disturbance and high gradients of dynamic film surface tension at the pore scale. Moreover, if P_c^* is still somewhat smaller than the average critical disjoining pressure of (mobile/stationary) foam films, the trapped gas is strongly influenced by the mobilization capillary number, defined as the ratio of the viscous to foam mobilization pressure gradients

$$N_c = \frac{\left|\nabla P_v(n_f, X_t, v_f)\right|}{\left|\nabla P_m(n_t, K)\right|} \tag{5}$$

where ∇P_v is the viscous gradient as a function of flowing-foam density n_f, fraction of trapped gas X_t, and the mean interstitial velocity of foam flow v_f. ∇P_m is the mobilization pressure gradient determined by the trapped gas density n_t and permeability K [Friedmann et al., 1991; Rossen, 1990]. Since n_f may also be dependent on v_f, ∇P_v might not considerably change with the variation of gas rate at P_c^*, in agreement with Khatib et al. [1988], who reported experimentally a quasi-linear relationship between the gas fractional flow and the

relative gas mobility in foam. As a result, the trapped gas fraction would be less sensitive to the gas rate for high quality foams at P_c^*, as found above.

3.10 Foam tracer transport in vertical Bentheim core

For horizontal flow, the highly mobile foam concentrates mainly in the upper part of the core, regardless of the gas rate, while the liquid rate apparently plays an important role in the mobilization of foam in the lower part. We surmise that gravity causes foam to be dryer towards the top of the core. As a result, foam in the upper region becomes less stable at the elevated gas rate, and thus the limiting capillary pressure governs its rheological behavior. On the contrary, increased liquid rate can increase in the liquid fraction of foam in the lower part of the core (particularly near the inlet region), resulting in low quality foam. To obtain a better understanding of the gravity effect, we next consider the distribution of foam mobilities in vertical flow.

Fig. 19 shows the displacement of Foam-A by Tracer-Foam-A in the central image plane at three different points in time. The high mobility foam cap observed with the horizontal flow (Fig. 15) is drastically modified as the foam flows vertically upwards.

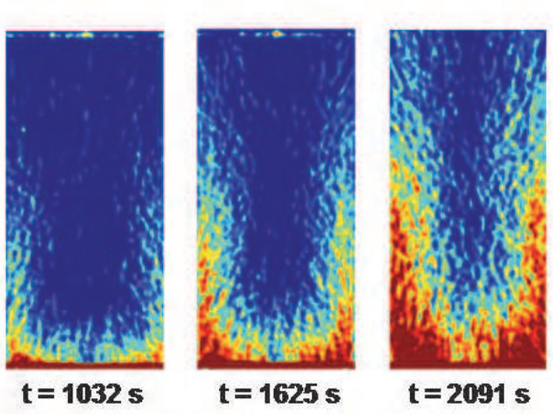

Fig. 19. Displacement of steady state nitrogen Foam-A (90.90 % quality) by the tracer foam in the vertical Bentheim core. The high foam mobility region has a 'cup'-shaped structure (outer annulus foam), leading to a higher total fraction of mobile foam, compared to the cap structure in the horizontal core (see Fig. 15).

The cap expands around the core center to form a symmetric annular shape, whose thickness slightly increases towards the inlet. Comparison with the images CP = 0 in Fig. 15 reveals that the tracer saturation is less variable for the vertical flow, suggesting a more uniform distribution of foam mobilities in the annular region (called outer-annulus foam). This is shown in the corresponding one-dimensional tracer saturation profiles shown in Fig. 20.

Consider the profiles at around 1000 seconds after injection of the tracer mixture for both core arrangements (Fig. 16a and 20), the tracer saturation for the vertical flow is about 5% higher in region 1, and decreases rapidly in region 2 to below 5% near the outlet, with a smoother transition between these regions. The profile at 1625 and 2091 seconds in Fig. 20 demonstrate the uniform slowdown of the rate of increase of tracer saturation, signaling most of the high mobility foams were displaced throughout the core. Note that the annular structure of the flowing foam region is expected to give a higher overall mobile foam

fraction than in the cap. However, this was not observed near the outlet region for the vertical flow where the mobile foam fraction was found to be lower. This conflicting result is most likely ascribed to a higher convective dispersion in the horizontal cap, which drove a relatively larger fraction of the high mobility foams to the outlet for a given elapsed time. Thus, it is appropriate to use the average quasi-stationary foam fractions for regions 1 and 2. For the profile at 2091 seconds in Fig. 45, $\overline{S}_t^1$ = 45 % and $\overline{S}_t^2$ = 70 %. These values are consistently lower than those for the horizontal foam flow determined at almost the same elapsed time.

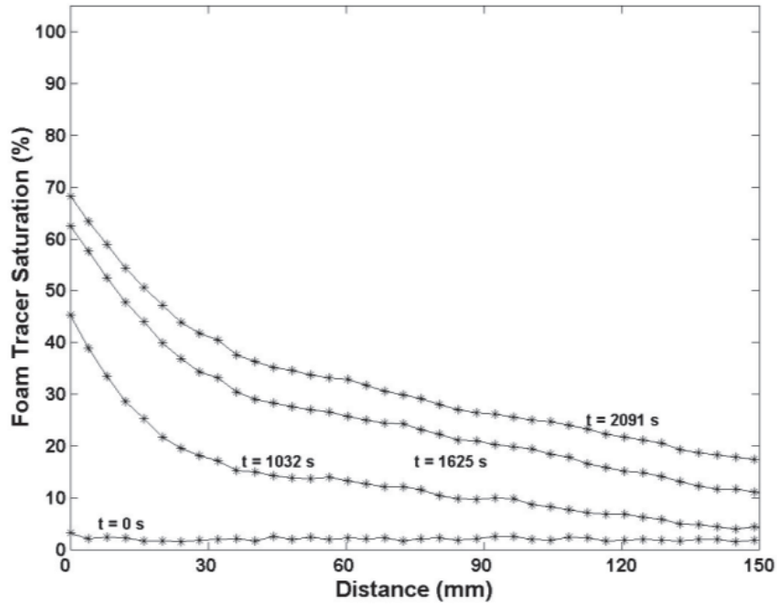

Fig. 20. One-dimensional foam-tracer saturation profile plotted versus distance from the inlet, during the displacement of the nitrogen Foam-A in the vertical Bentheim core (Fig 19).

4. Main conclusions

- The macroscopic conditions for foam propagation and the characteristic regimes of liquid flow in a quasi-stagnant foam matrix are crucial issues in the upscaled description of foam behavior in the majority of foam applications. These issues have been systematically investigated through the LDL and FDL processes, where the in-situ fluid mobility and partitioning are determined by the pressure drop measurement and the X-ray CT aided visualization. The theoretical and experimental framework elucidates several aspects that seem to be missing in the literature.
- For liquid displacement by foam, the pressure drop corresponds well with fluid saturation throughout a two-stage displacement. While the first stage has been commonly observed in previous work, the second stage seems to be a new phenomenon, which is characterized by a secondary liquid desaturation (SLD) initiating around the middle region of the core and propagating towards the inlet and outlet. Where and when the second saturation front emerges is important in designing a

field foam process. For instance, for foam-improved sweep efficiency or gas blockage in underground gas storage, the development of foam far way from injection wells is desired, whereas a strong foam development near the well-bore is essential for the success of foam induced acid diversion.

- Except the "entrance" effect, the two-stage liquid desaturation is not affected by the fluid rates. Unlike the "capillary-end" effect that is suppressed as the SLD emerges, the "entrance" effect is much more sensitive to the increase in the liquid rate than the gas rate. This is attributed to two factors: (1) foam generation by snap-off is dependent more on the liquid rate, and (2) the elevated gas rate results in a lower value of the limiting capillary pressure, as a refection of the well known detrimental effect of high gas rate on foam stability.
- For foam displacement by liquid, the conventional imbibition process changes substantially in the presence of foam. According to our theory, for an insignificant gas expansion and dissolution effect, the percolation of the liquid phase is determined not only by the injection rate, but also by the magnitude and uniformity of foam yield stresses, and the gravity effect. As a result, on the pore scale the "piston-like displacement" and/or the "wetting film" flow regimes are expected to characterize the imbibition process. This is consistent with most of the experimental results, which show both fingering- and dispersed-flow regimes on the macroscopic scale.
- The structure of the liquid finger associated with the trapped gas fraction is strongly influenced by the initial steady-state foam strength. Particularly, the finger becomes less tortuous and orientates upwards against gravity as the foam strength increases. As a result, the trapped gas fraction over the entire core at the quasi-steady state increases significantly (e.g. from 70.2 to 78.1% for surfactant-solution injection). Moreover, the fingering region encapsulates a significant gas fraction, which also increases with the foam strength (e.g. from 18.0 to 31.2% for surfactant-solution injection). Therefore, strong foam tends to hinder the "fingering-flow" regime, consistent with our simple theoretical analysis.
- The liquid rate has different effects on the fingering pattern. On one hand, the finger dimensions decrease with the liquid rate, but on the other hand, the gravity effect is aggravated.
- The inherent gas expansion obviously reduces the foam-mobilization pressure, and thus favors the 'fingering-flow" regime. This helps explain partially why the finger grows more laterally towards the inlet. An important practical implication of the gas expansion is that in a stratified formation, the gas expansion is normally faster in high permeability layers, potentially reducing the diversion capacity of foam in these layers. On the other hand, the gas expansion can also be resisted if it triggers foam generation. The latter is particularly true if the injected liquid is the surfactant solution.
- The experimental results have demonstrated that the X-ray CT aided tracer technique developed is a powerful tool for investigating foam-trapping phenomenon in porous media, as well as characterizing the micro-heterogeneity of the pore networks through different patterns of tracer convection-dispersion. The use of tracer concentration of 25 vol.% at 1 bar backpressure provides sufficient contrast between the tracer gas mixture (tracer foam) and the native gas (foam). A higher tracer concentration might be required for a lower system pressure, and vice versa.

- Since diffusion rate of the tracer in stationary foam is small, but not zero, a reliable interpretation of the in-situ tracer concentration profile can be obtained if convection dominates over diffusion. The dominant convection may increase the convective dispersion of the tracer, which modifies the actual distribution of the stationary and flowing components for a relatively short observation time. Therefore, the system length should be limited to ensure the consistency of the measured tracer concentration profile with the actual distribution of local fluid mobilities. If the system dimensions are large, the use of the regional concentration profiles is advisable.
- For the Bentheim sandstone core, the transient displacement of the tracer gas without foam demonstrates typical one-dimensional single-phase flow in a homogeneous medium. Foams strongly modify this flow pattern due to persistent and/or temporary foam trapping. For the horizontal core Foam-A with 90.9% quality shows its mobile fraction concentrated only in the upper half part of the core, with a small fluctuation of stationary foam very near the inlet in the lower part. An increase in foam quality up to 95.24% (by increasing the standard gas rate from 5 to 10 cm^3/min at a fixed liquid rate of 0.5 cm^3/min) primarily enhanced the mobility of the flowing foam and the fluctuation of stationary foam near the inlet region without a significant change of the macroscopic structure ($\overline{S_t^2}$ = 77% for Foam-A with 90.90% quality, 65% for Foam-B with 95.24% quality).
- The same trends for the mobility distribution to the variation of gas and liquid rates were also observed when the foams flowed vertically upwards. However, in this flow direction, for a given foam quality, the mobilities of flowing foams were reduced and rather uniformly distributed compared with the horizontal case. This resulted from the restructuring of the macroscopic pattern of foam mobility distribution in which the mobile foam formed an annular region, whose center was filled with quasi-stationary foam.
- The macroscopic quasi-stationary gas domain during the foam stage is distinctly different from that during the post-foam liquid injection. This is attributed to: (a) change in local equilibrium between foam generation and destruction, (b) gas expansion and dissolution, and (c) gravity effect.

5. Acknowledgment

I would like to thank Prof. Peter K. Currie and Prof. Pacelli Zitha for their valuable scientific discussions. I would also like to thank Shell for supporting this work.

6. References

Alvarez, R.E and Macovski, A.: "Energy-Selective Reconstructions in X-ray Computed Tomography," Phys. Med. Biol. (1976), 21, 733.

Alvarez, J.M.: "Foam-Flow Behaviour in Porous Media: Effects of Flow Regime and Porous-Medium Heterogeneity," PhD Dissertation (December) 1996, the university of Texas at Austin.

Apaydin, O.G. and Kovscek, A.R., "Transient Foam Flow in Homogeneous Porous Media: Surfactant Concentration and Capillary End Effects," SPE paper 59286 presented at the SPE/DOE Improved Oil Recovery Symposium, Tulsa, OK, 2000.

Behenna, F. R: "Acid Diversion from an Undamaged to a Damaged Core Using Multiple Foam Slugs," paper SPE 30121 presented at the SPE European Formation Damage Conference, The Hague, 1995.

Brooks, R.A., Weiss, G.H., and Talbert, A.J., J. Comput. Assist. Tomog. 1978, 2, 577.

Burganos, V.N., J. Chem. Phys. 1998, 109, 16, 6772.

Cheng, L, Kam, S.I., Delshad, M., and Rossen, W.R.: "Simulation of Dynamic Foam-Acid Diversion Process," paper SPE 68916 presented at the European Formation Damage Conference, The Hague, 2001.

Friedmann, F., Chen W.H., and Gauglitz, P.A.: "Experimental and Simulation Study of High-Temperature Foam Displacement in porous Media," SPE Reservoir Engineering 1991, 37.

Fulcher, Jr. R.A., Ertekin, T., and Stahl, C.D.: "Effect of Capillary Number and Its Constituents on Two-Phase Relative Permeability Curves," JPT 1985, 249.

Gauglitz, P.A., Friedmann, F., Kam, S. I., and Rossen, W. R.: "Foam Generation in Porous Media," paper SPE 75177 presented at the SPE/DOE Symposium on Improved Oil Recovery, Tulsa, OK, 2002.

Kak, A.C. and Roberts, B., in Handbook of Pattern Recognition and Image Processing, Young, T.Y. and Fu, K.S. (Eds.), New York Academic Press 1986.

Khatib, Z.I., Hirasaki, G.J., and Falls, A.H.: "Effects of Capillary Pressure on Coalescence and Phase Mobilities in Foam Flowing through Porous Media," SPE Reservoir Engineering 1988, 3, 919.

Kovscek, A.R., and Radke, C. J.: "Fundamentals of Foam Transport in Porous Media," in Foams: Fundamentals and Applications in the Petroleum Industry, ACS Advances in Chemistry series 242, Washington, DC (1994), 110.

Kibodeaux, K.R., Zeilinger, S.C., and Rossen, W.R.: "Sensitivity Study of Foam Diversion Process for Matrix Acidizing," paper SPE 28550 presented at the SPE Annual Technical Conference and Exhibition, New Orleans, LA, 1994.

McCullough, E.C., "Photon Attenuation in Computed Tomography" Med. Phys. 1975, 2, 307.

Millner, M., Payne, W.H., Waggener, R.G., McDavid, W.D., Dennis, M.J. and Sank, V.J., Med. Phys. 1978, 5, 543.

Osterloh, W.T. and Jante, M.J.: "Effects of Gas and Liquid Velocity on Steady-State Foam Flow," paper SPE 24179 presented at the SPE/DOE Symposium on Improved Oil Recovery, Tulsa, OK, 1992.

Parlar, M., Parris, M.D., Jasinski, R.J., Robert, J.A.: "An Experimental Study of Foam Flow Through Berea Sandstone with Applications to Foam Diversion in Matrix Acidizing," paper SPE 29678 presented at the SPE Western Regional Meeting, Bakerfield, CA, 1995.

Rossen, W.R. and Zhou, Z.H.: "Modeling Foam Mobility at the Limiting Capillary Pressure," SPE Advanced Technologies Series 1995, 3, 1.

Siddiqui, S., Talabani, S., Yang, J., Saleh, S., Islam, M.R.: "An Experimental Investigation of the Diversion Characteristics of Foam in Berea Sandstone Cores of Contrasting Permeability," paper SPE 37463 presented at the Production Operations Symposium, OK, 1997.

Tanzil, D., Hirasaki, G.J., and Miller, C.A.: "Conditions for Foam Generation in Homogeneous Porous Media," paper SPE 75176 presented at the SPE/DOE Symposium on Improved Oil Recovery, Tulsa, OK, 2002.

Thompson, K.E. and Gdanski, R.D.: "Laboratory Study Provides Guidelines for Diverting Acid with Foam," SPE Production & Facilities 1993.

Wassmuth, F.R., Green, K.A, and Randall, L.: "Details of In-situ Foam Propagation Exposed with Magnetic Resonance Imaging," SPE Reservoir Evaluation & Engineering 2001, 135.

Zerhboub, M., Ben-Naceur, K., Touboul, E, and Thomas, R.: "Matrix Acidizing: A Novel Approach to Foam Diversion," SPE Production & Facilities 1994.

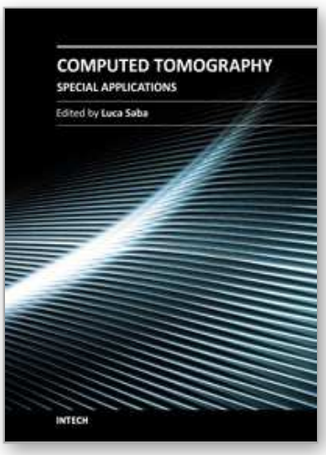

Computed Tomography - Special Applications
Edited by Dr. Luca Saba

ISBN 978-953-307-723-9
Hard cover, 318 pages
Publisher InTech
Published online 21, November, 2011
Published in print edition November, 2011

CT has evolved into an indispensable imaging method in clinical routine. The first generation of CT scanners developed in the 1970s and numerous innovations have improved the utility and application field of the CT, such as the introduction of helical systems that allowed the development of the "volumetric CT" concept. Recently interesting technical, anthropomorphic, forensic and archeological as well as paleontological applications of computed tomography have been developed. These applications further strengthen the method as a generic diagnostic tool for non destructive material testing and three dimensional visualization beyond its medical use.

InTech Europe
University Campus STeP Ri
Slavka Krautzeka 83/A
51000 Rijeka, Croatia
Phone: +385 (51) 770 447
Fax: +385 (51) 686 166
www.intechopen.com

InTech China
Unit 405, Office Block, Hotel Equatorial Shanghai
No.65, Yan An Road (West), Shanghai, 200040, China
中国上海市延安西路65号上海国际贵都大饭店办公楼405单元
Phone: +86-21-62489820
Fax: +86-21-62489821

IntechOpen